

# Control and amplification of Bloch oscillations via photon-mediated interactions

Haoqing Zhang,<sup>1,2</sup> Anjun Chu,<sup>1,2</sup> Chengyi Luo,<sup>1</sup> James K. Thompson,<sup>1</sup> and Ana Maria Rey<sup>1,2</sup>

<sup>1</sup>*JILA, NIST and Department of Physics, University of Colorado, Boulder, Colorado 80309, USA*

<sup>2</sup>*Center for Theory of Quantum Matter, University of Colorado, Boulder, Colorado 80309, USA*

(Dated: February 14, 2024)

We propose a scheme to control and enhance atomic Bloch oscillations via photon-mediated interactions in an optical lattice supported by a standing-wave cavity with incommensurate lattice and cavity wavelengths. Our scheme uses position-dependent atom-light couplings in an optical cavity to spatially prepare an array of atoms at targeted lattice sites starting from a thermal gas. On this initial state we take advantage of dispersive position-dependent atom-cavity couplings to perform non-destructive measurements of single-particle Bloch oscillations, and to generate long-range interactions self-tuned by atomic motion. The latter leads to the generation of dynamical phase transitions in the deep lattice regime and the amplification of Bloch oscillations in the shallow lattice regime. Our work introduces new possibilities accessible in state-of-the-art cavity QED experiments for the exploration of many-body dynamics in self-tunable potentials.

## I. INTRODUCTION

Bloch oscillations (BO) [1] are center-of-mass oscillations or coherent breathing experienced by independent particles in a periodic lattice potential in the presence of a constant force (e.g. gravity). Although it has been hard to directly control BO in conventional electron systems, they have been observed in tailored semiconductor systems [2] as well as ultracold atom systems trapped in optical lattices [3, 4]. Nevertheless, for the latter, the lattice potential is by implementation rigid and therefore not a good test bed example of the underlying physics in real materials where the phonons of the crystal dynamically interact with the electron motion. Furthermore, inter-atomic interactions have always been a competing mechanism which damp the oscillations.

Here we propose a scheme to control and amplify atomic BO via photon-mediated interactions in a gravity-tilted optical lattice supported by a standing-wave optical cavity with incommensurate lattice and cavity wavelengths. In our case, photons can actively modify the periodic potential experienced by the atoms and therefore resemble the role of phonons in a real solid state environment. Even though experiments that track BO in optical cavities have been implemented before using a Bose Einstein Condensate (BEC) [5–9], here we propose to use inhomogeneous atom-light couplings to prepare an array of atoms on specific lattice sites and initialize the dynamics [10]. This can be achieved via position-dependent dispersive atom-light couplings to map the motion of the atoms under BO into the frequency shift of the cavity resonance. Our protocol not only avoids the ultracold degenerate initial states required in non-destructive measurements of BO, but also provides flexible self-tunability of the cavity-mediated long-range interactions by the atomic motion. Moreover, in contrast to prior experiments where the periodic potential was generated by the probe laser field itself [5–9] or separate probe field for site-independent atom-light coupling [11], we use an additional lattice potential that traps the atoms and controls the degree

of delocalization of the underlying Wannier-Stark (WS) states [12] in our system. In this setting, different to the well-studied case of contact interactions [13–20], the photon-mediated interactions can modify BO depending on the position of other atoms in the array. Taking advantage of this feature we show versatile many-body phenomena can be realized in different parameter regimes of this system: In the deep lattice region, we find dynamical phase transitions (DPT) related to the Lipkin-Meshkov-Glick (LMG) model [21, 22], which potentially enables rapid generation of spin-squeezed states [23–25] with WS states directly, bypassing the need for Raman transitions [12]; In the shallow lattice, we find the amplification of Bloch oscillation amplification originating from the pair production [26–29] process from the central to adjacent WS states. We also discuss feasible implementations in state-of-the-art cavity QED experiments [30, 31].

## II. MODEL

We consider an ensemble of  $N$  ultracold atoms with mass  $M$  trapped in a standing-wave optical cavity along the vertical direction  $\hat{z}$  as shown in Fig. 1(a). The atoms are confined in the lowest band of the one-dimensional (1D) optical lattice supported by the cavity, with local gravitational acceleration  $\vec{g}$  generating an additional  $Mgz$  potential between sites separated by a vertical distance  $z$ . Here we consider the pure 1D model for simplicity and discuss the modification by the radial modes in [32]. A single internal level  $|g\rangle$  in the atomic ground manifold, is coupled to an atomic excited state  $|e\rangle$  with a transition energy  $\hbar\omega_0$  via a single cavity mode  $\hat{a}$  with frequency  $\omega_c$  and wavelength  $\lambda_c$ . The atom-cavity coupling has spatial dependence  $\mathcal{G}(z) = \mathcal{G}_0 \sin(k_c z)$ , where  $k_c = 2\pi/\lambda_c$  and  $\mathcal{G}_0$  is proportional to single atom vacuum Rabi splitting. The cavity mode is coherently driven by an additional laser with frequency  $\omega_p$  thus detuning  $\Delta_c = \omega_p - \omega_c$  from the bare cavity mode, which generates a net injected field in the cavity with amplitude  $\eta_p$ . The cavity has a finite linewidth  $\kappa$ .

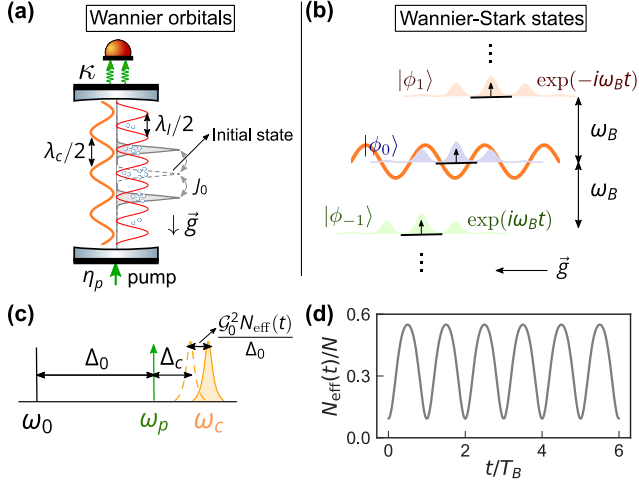


FIG. 1. Model system. (a) An ensemble of  $N$  atoms are trapped in the lowest band of an optical lattice supported by an optical cavity aligned with gravitational acceleration  $\vec{g}$ . Considering the atoms are initially localized in a Wannier orbital (grey dashed line), hopping to the nearby sites (grey solid line) can lead to a change of atom-cavity coupling due to incommensurate lattice ( $\lambda_l$ ) and cavity ( $\lambda_c$ ) wavelengths. The cavity has a finite linewidth  $\kappa$ . (b) The initially localized Wannier orbitals can also be written as a superposition of partially delocalized Wannier-Stark states which accumulate different phases due to gravity. (c) Frequencies of atomic transition ( $\omega_0$ ), external pump ( $\omega_p$ ) and cavity resonance ( $\omega_c$ ). Due to atomic motion, the cavity resonance will be shifted by  $\mathcal{G}_0^2 N_{\text{eff}}(t)/\Delta_0$ , with  $N_{\text{eff}}(t)$  defined in Eq. (3). (d)  $N_{\text{eff}}(t)$  displays oscillatory behavior reflecting single-particle atomic BO, generated by a sudden quench on lattice depth from  $15E_R$  to  $8E_R$ .

We work in the dispersive regime of the atom-light interaction, where both the cavity mode and the external drive are far detuned from the atomic resonance, i.e.,  $\Delta_0 \gg \mathcal{G}_0 \sqrt{\langle \hat{a}^\dagger \hat{a} \rangle}$  with  $\Delta_0 = \omega_p - \omega_0$ . In such limit, we can adiabatically eliminate the excited state and only consider the atomic motion in the ground state, which results in the following second-quantized Hamiltonian,

$$\hat{H} = \hat{H}_0 + \int dz \hat{\psi}_g^\dagger(z) \frac{\hbar |\mathcal{G}(z)|^2}{\Delta_0} \hat{a}^\dagger \hat{a} \hat{\psi}_g(z) + \hat{H}_{\text{cav}}, \quad (1)$$

where  $\hat{H}_0 = \int dz \hat{\psi}_g^\dagger (\hat{p}^2/2M + V_0 \sin^2(k_l z) + Mgz) \hat{\psi}_g$  includes the kinetic energy, lattice potential, and gravitational potential experienced by the atoms. Here,  $V_0$  is the lattice depth,  $k_l = 2\pi/\lambda_l$  is the wavenumber of the lattice beam that sets the atomic recoil energy  $E_R = \hbar^2 k_l^2/2M$ , where  $\lambda_l$  is the lattice wavelength. The field operator  $\hat{\psi}_g(z)$  annihilates a ground state atom at position  $z$ . The second term in Eq. (1) describes the dispersive atom-light coupling after the adiabatic elimination of the excited state. The cavity Hamiltonian is given by  $\hat{H}_{\text{cav}}/\hbar = -\Delta_c \hat{a}^\dagger \hat{a} + \eta_p \hat{a}^\dagger + \eta_p^* \hat{a}$ .

The eigenstates of  $\hat{H}_0$  are the so-called Wannier-Stark (WS) states. In the tight-binding limit, the wave function

for a WS state centered at lattice site  $n$  takes the form of  $\phi_n(z) = \sum_m \mathcal{J}_{m-n}(2J_0/Mga_l) w(z - ma_l)$  [12, 33], which is a superposition of localized ground-band Wannier functions  $w(z)$  [See Fig. 1(b)]. Here  $\mathcal{J}_n$  is the Bessel function of the first kind,  $J_0/\hbar$  is the nearest-neighbour tunneling rate, and  $a_l = \lambda_l/2$  is the lattice spacing. The eigenenergy of  $|\phi_n\rangle$  is  $n\hbar\omega_B$ , where  $\omega_B = Mga_l/\hbar$  is the Bloch frequency and  $T_B = 2\pi/\omega_B$  the corresponding Bloch period. We expand the field operator in the WS basis,  $\hat{\psi}_g(z) = \sum_n \hat{c}_n \phi_n(z)$ , where the operator  $\hat{c}_n$  annihilates an atom in the WS state  $\phi_n$ . In this basis, Eq. (1) can be rewritten as

$$\hat{H} = \hat{H}_{\text{cav}} + \frac{\hbar \mathcal{G}_0^2}{\Delta_0} \hat{a}^\dagger \hat{a} \hat{N}_{\text{eff}} + \hbar \omega_B \sum_n n \hat{c}_n^\dagger \hat{c}_n, \quad (2)$$

where

$$\hat{N}_{\text{eff}} = \sum_{m,n} J_{m,n} \hat{c}_m^\dagger \hat{c}_n. \quad (3)$$

Here,  $J_{m,n} = \int dz \phi_m(z) \phi_n(z) \sin^2(k_c z)$  describes the overlap between the WS states  $\phi_m, \phi_n$  weighted by the cavity field mode function.  $\hat{N}_{\text{eff}}$  can be understood as the effective number of atoms coupled to the cavity, which are responsible for generating a frequency shift  $\mathcal{G}_0^2 N_{\text{eff}}/\Delta_0$  on the cavity resonance, where  $N_{\text{eff}} = \langle \hat{N}_{\text{eff}} \rangle$ . This dispersive term allows us to either perform non-destructive probing or many-body control of the atomic motion, depending on the operating parameter regime.

Assuming the cavity field adiabatically follows the atomic motion, which is valid since the cavity field dynamics ( $\Delta_c \sim \text{MHz}$ ) is much faster than the time evolution of the atomic field ( $\omega_B \sim \text{kHz}$ ), one can replace the cavity field operator by  $\hat{a} \approx \eta_p/(\Delta_c - \mathcal{G}_0^2 \hat{N}_{\text{eff}}/\Delta_0)$ . This leads to the following effective atom-only Hamiltonian [32],

$$\hat{H}_{\text{eff}}/\hbar = \omega_B \sum_n n \hat{c}_n^\dagger \hat{c}_n + \hat{V}_{\text{cav}}(\hat{N}_{\text{eff}}), \quad (4)$$

where  $\hat{V}_{\text{cav}}(\hat{N}_{\text{eff}}) = -(VN/\beta)/(1 + \beta \hat{N}_{\text{eff}}/N)$  is the cavity-induced potential depending on the atomic motion. Here,  $V = \mathcal{G}_0^2 |\eta_p|^2/(\Delta_c^2 \Delta_0)$  is the maximum AC Stark shift on the atoms introduced by the bare cavity mode,  $\beta = -N\mathcal{G}_0^2/(\Delta_0 \Delta_c)$  is the ratio between the maximum cavity shift and the bare cavity detuning. We assume  $\beta > 0$  ( $\Delta_0$  and  $\Delta_c$  have opposite signs) to avoid hitting a cavity resonance.

### III. SINGLE-PARTICLE DYNAMICS

First we consider the simplest case where the cavity is used as a probe and does not affect the single-particle dynamics set by  $\hat{H}_0$ , valid in the regimes  $V \ll \omega_B$ . We consider the case where atoms are initially loaded in an almost localized WS state in a deep lattice at sites  $n$  minimally coupled to the cavity ( $k_n a_l/\pi = r$  with  $n, r \in \mathbb{Z}$ ).

Then we suddenly quench the lattice depth to a shallow depth, and the atoms start hopping to the nearest-neighbour sites [see Fig. 1(a)]. Since the initially localized state corresponds to a superposition of WS states of the shallow lattice [see Fig. 1(b)], after the quench, each WS state acquires a phase that evolves at a rate set by  $\omega_B$ . The interference of different WS states induces tunneling away from the initially populated site, resulting in coherent breathing behavior at the BO frequency  $\omega_B$ .

To probe the BO, we use the fact that atoms at different sites coupled differently to the cavity. Therefore tunneling out and back into the initial site leads to a periodic oscillation in  $N_{\text{eff}}(t)$  at frequency  $\omega_B$  as shown in Fig. 1(d), which can be measured by tracking the cavity frequency shift  $\mathcal{G}_0^2 N_{\text{eff}}(t)/\Delta_0$ . Note that a technique to initially prepare atoms at lattice sites with low initial coupling to the cavity mode has been demonstrated in [10]. Instead of an initially localized state, we can also use amplitude modulation of the lattice depth [19] to prepare a superposition of WS states. In this case a similar behavior can be observed as detailed in [32].

For the numerical simulations throughout this letter, we consider the case of  $^{87}\text{Rb}$  atoms with cavity wavelength  $\lambda_c = 780$  nm and lattice wavelength  $\lambda_l = 532$  nm. However, the discussion can be easily adapted to other type of atoms discussed in [32].

#### IV. DEEP LATTICE REGIME

The interplay between single-particle atomic motion and cavity-mediated interactions occurs if  $V \sim \omega_B$ . Here we focus on the deep lattice regime ( $V_0 = 20E_R$ ) where WS states are almost localized at individual lattice sites. If atoms are prepared at site  $n = 0$ , and  $V > 0$ , the differential cavity induced AC Stark shift (first order in  $\beta$  in the limit  $\beta \ll 1$ ) between the  $n = 0$  and  $n = -1$  sites  $\propto V(J_{0,0} - J_{-1,-1})$  can compensate for their energy difference  $\hbar\omega_B$  as shown in Fig. 2(a), restoring tunnelling between these two sites. Since the atomic motion is restricted to take place between these two states, we map them to an effective spin 1/2 degree of freedom:  $\hat{c}_{-1}$  as  $\hat{c}_{\uparrow}$ ,  $\hat{c}_0$  as  $\hat{c}_{\downarrow}$  as well as the spin operators  $\hat{S}_z = (\hat{c}_{\uparrow}^\dagger \hat{c}_{\uparrow} - \hat{c}_{\downarrow}^\dagger \hat{c}_{\downarrow})/2$ ,  $\hat{S}_x = (\hat{c}_{\uparrow}^\dagger \hat{c}_{\downarrow} + \hat{c}_{\downarrow}^\dagger \hat{c}_{\uparrow})/2$ . Thus we have  $\hat{N}_{\text{eff}} = 2(\Delta_{-1}\hat{S}_z + \Omega_{-1}\hat{S}_x) + N\bar{\omega}$ , where  $\Delta_{-1} = (J_{-1,-1} - J_{0,0})/2$ ,  $\Omega_{-1} = J_{-1,0}$ , and  $\bar{\omega} = (J_{-1,-1} + J_{0,0})/2$ .

In the limit of  $\beta \ll 1$ , one can expand  $\hat{H}_{\text{eff}}$  [Eq. (4)] in a power series of  $\beta$ , and keep only the leading order terms. The Hamiltonian simplifies to,

$$\hat{H}_{\text{eff}}/\hbar \approx -\omega_B \hat{S}_z + V \hat{N}_{\text{eff}} - \frac{V\beta}{N} \hat{N}_{\text{eff}}^2. \quad (5)$$

This approximated Hamiltonian [Eq. (5)] is equivalent to the LMG model [12, 21–25, 32, 34],  $H_{\text{LMG}} = \chi \hat{S}_z^2 + \tilde{\Omega} \hat{S}_x - \tilde{\delta} \hat{S}_z$ , by a rotation along the  $y$ -axis of the Bloch

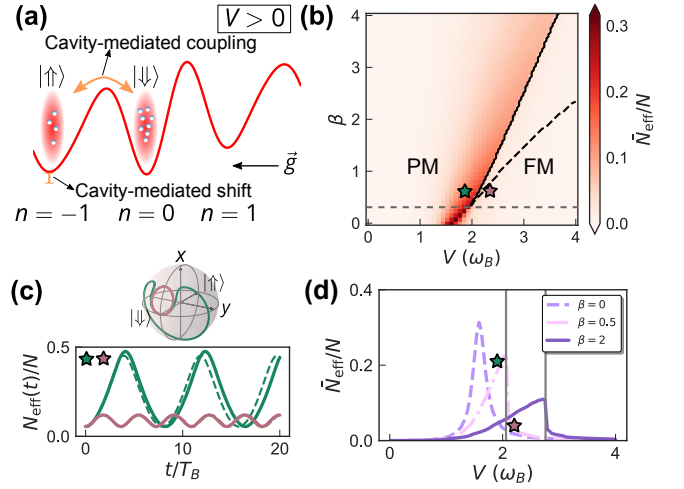


FIG. 2. Dynamical Phase Transition (DPT) in the deep lattice regime ( $V_0 = 20E_R$ ). (a) For the case of  $V > 0$  we define an effective spin-1/2 degrees of freedom:  $|\uparrow\rangle$  ( $|\phi_{-1}\rangle$ ) and  $|\downarrow\rangle$  ( $|\phi_0\rangle$ ). The cavity-mediated interactions generate energy shifts to balance the potential energy of these two sites (red curve), as well as dynamical couplings between them (orange arrow). (b) Phase diagram of the DPT determined by the long-time average  $\bar{N}_{\text{eff}}/N$ . The phase boundary separating the paramagnetic (PM) and ferromagnetic (FM) phase is predicted by the full model (solid line) and LMG model (black dashed line). The smooth crossover regime is below the gray dashed line. (c) Mean-field dynamics with  $V = 1.9\omega_B$ ,  $\beta = 0.5$  (green) and  $V = 2.2\omega_B$ ,  $\beta = 0.5$  (red). The upper panel shows the mean-field trajectories on the Bloch sphere, and the lower panel displays the normalized signal  $N_{\text{eff}}(t)/N$ . The solid (dashed) line show predictions of the full (LMG) model respectively. (d) Horizontal cut of the phase diagram in (b) for  $\beta = 0$  (solid),  $\beta = 0.5$  (dashed),  $\beta = 2$  (dot dashed).

sphere,  $\hat{S}_\alpha = \hat{R}^\dagger \hat{S}_\alpha \hat{R}$ , where  $\hat{R} = \exp(i\theta \hat{S}_y)$ , and  $\tan \theta = \Delta_{-1}/\Omega_{-1}$  [32], which enables fast entanglement state generation under particular choice of  $\chi, \tilde{\Omega}, \tilde{\delta}$  [23–25]. The LMG model features a DPT from a dynamical ferromagnetic (FM) to a dynamical paramagnetic phase (PM), signaled by a sharp change in the behavior of the long-time average of the excitation fraction [21, 22]. In our model [Eq. (4)], the long-time average of the signal  $\bar{N}_{\text{eff}}/N = \lim_{T \rightarrow \infty} \int_0^T dt N_{\text{eff}}(t)/(TN)$  plays the role of the dynamical order parameter. We also show that the DPT exists in our model [Eq. (4)] even beyond the  $\beta \ll 1$  limit as we discuss below.

To find the DPT, we solve the mean-field equations of motion for  $s_{x,y,z} = 2\langle \hat{S}_{x,y,z} \rangle/N$ . Such non-linear dynamics can be further reduced to  $(\dot{N}_{\text{eff}}/N)^2 + f(N_{\text{eff}}/N) = 0$  with  $f(J_{0,0}) = 0$ , and we can associate the DPT with an abrupt change in the number of real roots of the effective potential  $f(N_{\text{eff}}/N)$  [32]. This leads to the distinct dynamical behaviors of  $N_{\text{eff}}/N$  tuned by varying  $V$  and  $\beta$  as shown in Fig. 2(b,c,d). When the dynamics are dominated by interaction effects, the system is in the FM phase where the Bloch vector features small oscillations

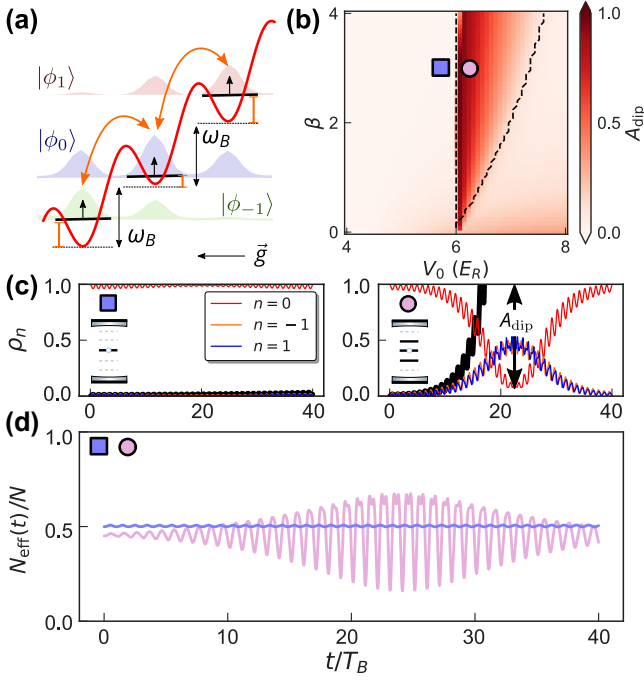


FIG. 3. Cavity-mediated amplification of Bloch oscillations in the shallow lattice regime. (a) The red lines show the gravity plus optical lattice potential. Around  $V_0 \approx 6E_R$ , WS states can extend to the nearest-neighbour lattice sites. The orange vertical lines represent the cavity-induced onsite shift of the energy levels and the orange arrows illustrate the cavity-mediated tunneling process shown in Eq. (6). (b) Transition between amplification regime and normal regime indicated by  $A_{\text{dip}} = 1 - \min\{\rho_0\}$ .  $V$  is fixed to be  $2\omega_B$ . The black dashed line shows the predicted boundary from UPA. (c) Mean-field dynamics of  $\rho_n$  with initial state  $|\phi_0\rangle$  and  $V = 2\omega_B, \beta = 3$ . Nearly no dynamics happen in the left panel (purple square,  $V_0 = 5.8E_R$ ) while large population transfer to  $|\phi_1\rangle$  and  $|\phi_{-1}\rangle$  (pink circle,  $V_0 = 6.2E_R$ ) is observed in the right panel. (d) Mean-field simulations for the normalized signal  $N_{\text{eff}}(t)/N$  for the same parameters described in (c). The purple line stays almost constant while the pink line signals the cavity enhancement of the BO.

around the south pole, also shown as small amplitude oscillations in  $N_{\text{eff}}(t)/N$ . This phase is separated by a DPT to a PM phase where the Bloch vector exhibits large excursions around the Bloch sphere, also shown as large amplitude oscillations in  $N_{\text{eff}}(t)/N$ . For  $\beta < 0.32$  [32], the DPT transforms into a smooth crossover and the dynamics becomes dominated by single-particle tunneling processes. The dynamical phase boundary is plotted in Fig. 2(b) with the full model (solid line) and the LMG model (dashed line). The LMG model is unable to capture the phase boundary beyond the  $\beta \ll 1$  limit.

## V. SHALLOW LATTICE REGIME

In a shallow lattice, the WS states extend over a few adjacent lattice sites. In this case, one can obtain a significant suppression of differential AC Stark shifts generated by the cavity by operating near the so-called magic lattice depth ( $V_0 = 6E_R$  for the Rb parameters we use) [12], where  $J_{n,n}$  is nearly a constant and the energy difference between nearest-neighbour WS states is roughly  $\hbar\omega_B$  [see Fig. 3(a)]. Thus the dynamics features BO even in the presence of strong cavity-mediated interactions. In fact, after preparing the atoms in the WS state  $|\phi_0\rangle$  and thus in an eigenstate of the single particle Hamiltonian, one can observe the generation and amplification of BO due to cavity-mediated interactions in a window around the magic depth as shown in Fig. 3(b,c,d). Since the short-time dynamics occurs mainly between the WS states centered at  $n = 0, \pm 1$ , we can concentrate only on these states and simplify the dynamics via the undepleted pump approximation (UPA): To the leading order, one can replace the operators for the initially occupied states as c-numbers,  $\hat{c}_0, \hat{c}_0^\dagger \sim \sqrt{N}$ , and keep the operators for unoccupied states ( $\hat{c}_{\pm 1}, \hat{c}_{\pm 1}^\dagger$ ) to the second order while absorbing the linear term generated by single-particle tunneling via a displacement of a coherent state,  $\hat{c}_{\pm 1} = \alpha_{\pm 1} + \tilde{c}_{\pm 1}$ . In this way,  $\hat{H}_{\text{eff}}$  [Eq. (4)] simplifies into a quadratic form [32],

$$\begin{aligned} \hat{H}_{\text{eff}}/\hbar \approx & \omega_B(\tilde{c}_1^\dagger \tilde{c}'_1 - \tilde{c}_{-1}^\dagger \tilde{c}'_{-1}) + V_1 \Delta(\tilde{c}_1^\dagger \tilde{c}'_1 + \tilde{c}_{-1}^\dagger \tilde{c}'_{-1}) \\ & + V_2 N \Omega^2 (\tilde{c}_1^\dagger + \tilde{c}'_1 - \tilde{c}_{-1}^\dagger - \tilde{c}'_{-1})^2, \end{aligned} \quad (6)$$

with the expansion coefficient  $V_1, V_2$  in [32] and  $\Delta = \Delta_1 \approx \Delta_{-1}, \Omega = \Omega_1 \approx -\Omega_{-1}$ .

We analyze the exact dynamics of Eq. (6) via the Bogoliubov-de Gennes method, in which the Heisenberg equation of motion for operators  $\hat{C} = (\tilde{c}_1^\dagger, \tilde{c}_{-1}^\dagger, \tilde{c}_1, \tilde{c}_{-1})^T$  takes the form  $i\partial_t \hat{C} = \mathcal{H}_{\text{BdG}} \hat{C}$ . The matrix  $\mathcal{H}_{\text{BdG}}$  can have either real or complex eigenvalues, which leads to distinct dynamical behaviors as shown in Fig. 3(c). When all the eigenvalues are real (normal regime), the populations  $\rho_0$  and  $\rho_{\pm 1}$ , with  $\rho_n = \langle \hat{c}_n^\dagger \hat{c}_n \rangle$ , feature stable small amplitude oscillations; on the other hand when all the eigenvalues are complex, then  $\rho_{\pm 1}$  feature an exponential growth associated with the correlated pair production of atoms at WS centered at  $n = \pm 1$ , which leads to the amplification of the BO signal until UPA breaks down. The transition between the real and complex eigenvalues of  $\mathcal{H}_{\text{BdG}}$  is marked by dashed lines in Fig. 3(b).

To quantify the population transfer, we define  $A_{\text{dip}} = 1 - \min\{\rho_0\}$  with  $\min\{\rho_0\}$  as the minimum of  $\rho_0$  during  $t \in [0, 40T_B]$ . A large  $A_{\text{dip}}$  signals efficient population transfer. In Fig. 3(b), we show  $A_{\text{dip}}$  as a function of the lattice depth  $V_0$  and the cavity parameter  $\beta$ . The region of amplified BO lies within the two dashed boundaries. The left boundary is fixed at the magic lattice depth ( $V_0 = 6E_R$ ) and the right boundary pushes to larger  $\beta$  as  $V_0$  increases. Inside the amplification region  $A_{\text{dip}} \neq$



0, while outside  $A_{\text{dip}} \approx 0$ . The evolution of  $N_{\text{eff}}(t)/N$  is shown in Fig. 3(d), where the enhanced population transfer induced by the cavity-mediated interactions lead to the growth of the BO amplitude in the amplification regime.

## VI. EXPERIMENTAL CONSIDERATION

The predicted behavior should be achievable in state-of-the-art cavity QED systems with  $N \sim 10^4$   $^{87}\text{Rb}$  atoms. We focus on the unitary dynamics in this letter while the main decoherence sources come from cavity loss and spontaneous emission from the excited states. The cavity loss generates collective dephasing processes at a rate  $V\beta\kappa/\Delta_c$  and spontaneous emission generates off-resonant photon scattering processes at a rate  $V\gamma/\Delta_0$ , where  $\gamma$  is the spontaneous emission rate. For an optical cavity with cooperativity  $C = 4\mathcal{G}_0^2/\gamma\kappa \sim 0.5$ ,  $\kappa/\Delta_c \sim 0.05$ ,  $\gamma/\Delta_0 \sim 0.01$ , one obtains negligible dissipation within experimentally relevant time scales ( $\sim 50$  BO periods). Our scheme does not require BEC while utilizes site-selection to prepare the initial state, which is robust to the radial thermal noise up to  $T \sim 1\mu\text{K}$  [32]. Contact interactions between atoms can also be ignored for the dilute quantum gas used here ( $\sim 50$  atoms per site). Moreover, our model can be realized with other species of alkali atoms ( $D_2$  transition) and alkaline earth atoms ( $^1S_0 \rightarrow ^3P_1$  transition) with appropriate choices of lattice wavelength [32]. In particular, contact interactions can be further suppressed using  $^{88}\text{Sr}$  atoms featuring negligible scattering lengths or any type of fermionic atoms interacting only via the  $p$ -wave channel.

## VII. CONCLUSION AND OUTLOOK

In summary, we proposed a scheme to perform many-body control of atomic BO in an optical cavity. Our work opens new possibilities for Hamiltonian engineering in many-body systems by taking advantage of the interplay between atomic motion, gravity and cavity-mediated interactions. For example, although so far we only focused on a single internal level, by including more levels and more cavity modes, it should be possible to engineer dynamical self-generated couplings between WS states via cavity-mediated interactions, which could be used to study dynamical gauge field [35–37] in a synthetic ladder without the overhead of Raman beams. Furthermore, although most of the calculations so far have been limited to regimes where the mean-field dynamics are a good description of the system, by loading the atoms in 2D or 3D lattice, one should be able to increase the role of beyond mean-field effects and enter the regimes where quantum correlations dominate the dynamics.

## ACKNOWLEDGMENTS

We thank Tianrui Xu and Tobias Bothwell for critical reading of the manuscript, and we thank Helmut Ritsch for useful discussions. This work is supported by the AFOSR Grant No. FA9550-18-1-0319, by the DARPA (funded via ARO) Grant No. W911NF-16-1-0576, the ARO single investigator Grant No. W911NF-19-1-0210, the NSF PHY1820885, NSF JILA-PFC PHY-1734006 and NSF QLCI-2016244 grants, by the DOE Quantum Systems Accelerator (QSA) grant and by NIST.

- 
- [1] F. Bloch, *Zeitschrift für physik* **52**, 555 (1929).
  - [2] C. Waschke, H. G. Roskos, R. Schwedler, K. Leo, H. Kurz, and K. Köhler, *Physical review letters* **70**, 3319 (1993).
  - [3] M. B. Dahan, E. Peik, J. Reichel, Y. Castin, and C. Salomon, *Physical Review Letters* **76**, 4508 (1996).
  - [4] B. P. Anderson and M. A. Kasevich, *Science* **282**, 1686 (1998).
  - [5] H. Keßler, J. Klinder, B. P. Venkatesh, C. Georges, and A. Hemmerich, *New Journal of Physics* **18**, 102001 (2016).
  - [6] C. Georges, J. Vargas, H. Keßler, J. Klinder, and A. Hemmerich, *Physical Review A* **96**, 063615 (2017).
  - [7] B. M. Peden, D. Meiser, M. L. Chiofalo, and M. J. Holland, *Phys. Rev. A* **80**, 043803 (2009).
  - [8] B. P. Venkatesh, M. Trupke, E. A. Hinds, and D. H. J. O'Dell, *Physical Review A* **80**, 063834 (2009).
  - [9] B. P. Venkatesh and D. H. J. O'Dell, *Phys. Rev. A* **88**, 013848 (2013).
  - [10] B. Wu, G. P. Greve, C. Luo, and J. K. Thompson, *arXiv:2104.01201* (2021).
  - [11] R. D. Niederriter, C. Schlupf, and P. Hamilton, *Physical Review A* **102**, 051301 (2020).
  - [12] A. Chu, P. He, J. K. Thompson, and A. M. Rey, *Physical Review Letters* **127**, 210401 (2021).
  - [13] A. Buchleitner and A. R. Kolovsky, *Physical review letters* **91**, 253002 (2003).
  - [14] A. R. Kolovsky, *Physical review letters* **90**, 213002 (2003).
  - [15] D. Witthaut, M. Werder, S. Mossmann, and H. Korsch, *Physical Review E* **71**, 036625 (2005).
  - [16] T. Schulte, S. Drenkelforth, G. K. Büning, W. Ertmer, J. Arlt, M. Lewenstein, and L. Santos, *Physical Review A* **77**, 023610 (2008).
  - [17] S. Walter, D. Schneble, and A. C. Durst, *Physical Review A* **81**, 033623 (2010).
  - [18] F. Meinert, M. J. Mark, E. Kirilov, K. Lauber, P. Weinmann, M. Gröbner, and H.-C. Nägerl, *Physical Review Letters* **112**, 193003 (2014).
  - [19] A. Alberti, G. Ferrari, V. V. Ivanov, M. L. Chiofalo, and G. M. Tino, *New Journal of Physics* **12**, 065037 (2010).
  - [20] L. Masi, T. Petrucciani, G. Ferioli, G. Semeghini, G. Modugno, M. Inguscio, and M. Fattori, *Physical Review Letters* **127**, 020601 (2021).
  - [21] A. Chu, J. Will, J. Arlt, C. Klempt, and A. M. Rey, *Physical Review Letters* **125**, 240504 (2020).

- [22] J. A. Muniz, D. Barberena, R. J. Lewis-Swan, D. J. Young, J. R. K. Cline, A. M. Rey, and J. K. Thompson, *Nature* **580**, 602 (2020).
- [23] J. Ma, X. Wang, C.-P. Sun, and F. Nori, *Physics Reports* **509**, 89 (2011).
- [24] L. Pezzè, A. Smerzi, M. K. Oberthaler, R. Schmied, and P. Treutlein, *Reviews of Modern Physics* **90**, 035005 (2018).
- [25] Z. Li, S. Colombo, C. Shu, G. Velez, S. Pilatowsky-Cameo, R. Schmied, S. Choi, M. Lukin, E. Pedrozo-Peñafiel, and V. Vuletić, *arXiv:2212.13880* (2022).
- [26] C. Gross, H. Strobel, E. Nicklas, T. Zibold, N. Bar-Gill, G. Kurizki, and M. Oberthaler, *Nature* **480**, 219 (2011).
- [27] B. Lücke, M. Scherer, J. Kruse, L. Pezzé, F. Deuretzbacher, P. Hyllus, O. Topic, J. Peise, W. Ertmer, J. Arlt, et al., *Science* **334**, 773 (2011).
- [28] A. Periwal, E. S. Cooper, P. Kunkel, J. F. Wienand, E. J. Davis, and M. Schleier-Smith, *Nature* **600**, 630 (2021).
- [29] F. Finger, R. Rosa-Medina, N. Reiter, P. Christodoulou, T. Donner, and T. Esslinger, *arXiv:2303.11326* (2023).
- [30] C. D. Panda, M. Tao, J. Egelhoff, M. Ceja, V. Xu, and H. Müller, *arXiv:2210.07289* (2022).
- [31] C. Luo, H. Zhang, V. P. Koh, J. D. Wilson, A. Chu, M. J. Holland, A. M. Rey, and J. K. Thompson, *arXiv:2304.01411* (2023).
- [32] See Supplemental Material at [URL will be inserted by publisher] for details of effective Hamiltonian derivation, dynamical phase transition, undepleted pump approximation and experimental implementation, includes Ref. [12, 19, 21, 22, 38].
- [33] M. Glück, A. R. Kolovsky, and H. J. Korsch, *Physics Reports* **366**, 103 (2002).
- [34] A. Aeppli, A. Chu, T. Bothwell, C. J. Kennedy, D. Kedar, P. He, A. M. Rey, and J. Ye, *Science Advances* **8**, eadc9242 (2022).
- [35] F. Mivehvar, F. Piazza, T. Donner, and H. Ritsch, *Advances in Physics* **70**, 1 (2021).
- [36] E. Colella, A. Kosior, F. Mivehvar, and H. Ritsch, *Physical Review Letters* **128**, 070603 (2022).
- [37] R. Rosa-Medina, F. Ferri, F. Finger, N. Dogra, K. Kroeger, R. Lin, R. Chitra, T. Donner, and T. Esslinger, *Physical Review Letters* **128**, 143602 (2022).
- [38] K. C. Cox, G. P. Greve, B. Wu, and J. K. Thompson, *Physical Review A* **94**, 061601 (2016).

# Control and amplification of Bloch oscillations via photon-mediated interactions: Supplemental Materials

Haoqing Zhang,<sup>1,2</sup> Anjun Chu,<sup>1,2</sup> Chengyi Luo,<sup>1</sup> James K. Thompson,<sup>1</sup> and Ana Maria Rey<sup>1,2</sup>

<sup>1</sup>*JILA, NIST and Department of Physics, University of Colorado, Boulder, Colorado 80309, USA*

<sup>2</sup>*Center for Theory of Quantum Matter, University of Colorado, Boulder, Colorado 80309, USA*

(Dated: February 14, 2024)

## S1. CAVITY QED WITH WANNIER-STARK STATE

### A. Dispersive coupling between atoms and cavity

In the main text, we considered  $N$  ultracold atoms trapped in a standing-wave optical cavity along the vertical direction  $\hat{z}$ . The atoms are assumed to be confined in the ground band of the one-dimensional lattice with lattice depth  $V_0$  and wave vector  $k_l = 2\pi/\lambda_l$ . A single internal level  $|g\rangle$  in the atomic ground manifold is coupled to an atomic excited state  $|e\rangle$  with a transition energy  $\hbar\omega_0 = \hbar(\omega_e - \omega_g)$ , via a single cavity mode  $\hat{a}$  with angular frequency  $\omega_c$  and wavelength  $\lambda_c$ . The atom-cavity coupling has spatial dependence  $\mathcal{G}(z) = \mathcal{G}_0 \sin(k_c z)$ , with  $k_c = 2\pi/\lambda_c$ . The cavity mode is coherently driven by an external light field with detuning  $\Delta_c = \omega_p - \omega_c$  from the bare cavity mode, which generates a net injected field in the cavity with amplitude  $\eta_p$ . The full atom-cavity Hamiltonian is given as  $H = \hat{H}_{\text{atom}} + \hat{H}_{\text{light}} + \hat{H}_{\text{int}}$ . each of the terms can be written as :

$$\hat{H}_{\text{light}} = \hbar(\eta_p \hat{a}^\dagger e^{-i\omega_p t} + \eta_p^* \hat{a} e^{i\omega_p t}) + \hbar\omega_c \hat{a}^\dagger \hat{a} \quad (\text{S1})$$

$$\hat{H}_{\text{atom}} = \sum_{\tau=g,e} \int dz \hat{\psi}_\tau^\dagger(z) \left[ \frac{p^2}{2M} + V(z) + \hbar\omega_\tau \right] \hat{\psi}_\tau(z) \quad (\text{S2})$$

$$\hat{H}_{\text{int}} = \hbar \int dz \mathcal{G}_0 \sin k_c z \left[ \hat{a} \hat{\psi}_e^\dagger(z) \hat{\psi}_g(z) + \hat{a}^\dagger \hat{\psi}_g^\dagger(z) \hat{\psi}_e(z) \right]. \quad (\text{S3})$$

Here  $V(z) = Mgz + V_0 \sin^2 k_l z$  describes the external potentials experienced by the atoms.  $\hat{\psi}_{e(g)}^\dagger(z)$  is the field operator that creates an atom in the state  $e(g)$  at position  $z$ ,  $\omega_{e(g)}$ . Under the rotating frame of the pump field (set by the Hamiltonian  $H_0 = \hbar\omega_p \hat{a}^\dagger \hat{a} + \hbar\omega_p \int dz \hat{\psi}_e^\dagger(z) \hat{\psi}_e(z)$ ), the system's Hamiltonian takes the following form:

$$\hat{H} = \hbar(\eta_p \hat{a}^\dagger + \eta_p^* \hat{a}) - \Delta_c \hat{a} \hat{a}^\dagger \hat{a} - \hbar\Delta_0 \int dz \hat{\psi}_e^\dagger(z) \hat{\psi}_e(z) + \sum_{\tau=g,e} \int dz \hat{\psi}_\tau^\dagger(z) \left[ \frac{p^2}{2M} + V(z) \right] \hat{\psi}_\tau(z) \quad (\text{S4})$$

$$+ \hbar \int dz \mathcal{G}_0 \sin k_c z \left[ \hat{a} \hat{\psi}_e^\dagger(z) \hat{\psi}_g(z) + \hat{a}^\dagger \hat{\psi}_g^\dagger(z) \hat{\psi}_e(z) \right], \quad (\text{S5})$$

where we defined the detuning of the pump from the atomic transition as  $\Delta_0 = \omega_p - \omega_0$ .

Furthermore, under the assumption  $\Delta_0 \gg \mathcal{G}_0 \sqrt{\langle \hat{a}^\dagger \hat{a} \rangle}$  and  $\Delta_0 \gg \gamma$  with  $\gamma$  the excited state spontaneous emission rate, the excited state population remains negligible during the relevant time scales. In this limit we can adiabatic eliminate the excited state  $|e\rangle$  ( $\hat{\psi}_e(z) \approx \mathcal{G}_0 \hat{a} \hat{\psi}_g(z) \sin k_c z / \Delta_0$ ), which leads to the following effective Hamiltonian acting on the ground state  $|g\rangle$  manifold only,

$$\hat{H} = -\hbar\Delta_c \hat{a}^\dagger \hat{a} + \hbar(\eta_p \hat{a}^\dagger + \eta_p^* \hat{a}) + \int dz \hat{\psi}_g^\dagger(z) \left[ \frac{\hbar(\mathcal{G}_0 \sin k_c z)^2}{\Delta_0} \hat{a}^\dagger \hat{a} + \frac{p^2}{2M} + V(z) \right] \hat{\psi}_g(z). \quad (\text{S6})$$

In the tight-binding limit, the resulting single-particle eigenstates of the Hamiltonian  $p^2/2m + V(z)$  become the so-called Wannier-Stark (WS) states  $|\phi_n\rangle$  ( $n \in \mathbb{Z}$ ):

$$E_n = Mga_l n, \quad \phi_n(z) = \sum_m \mathcal{J}_{m-n} \left( \frac{2J_0}{Mga_l} \right) w(z - ma_l). \quad (\text{S7})$$

Here  $\mathcal{J}_n$  denotes the Bessel function of the first kind,  $J_0$  denotes the nearest-neighbor couplings in the ground band,  $a_l = \lambda_l/2$  is the lattice spacing and  $w(z)$  is the ground band Wannier function. We will also use  $E_R = (\hbar k_l)^2/2M$  for the atomic recoil energy.

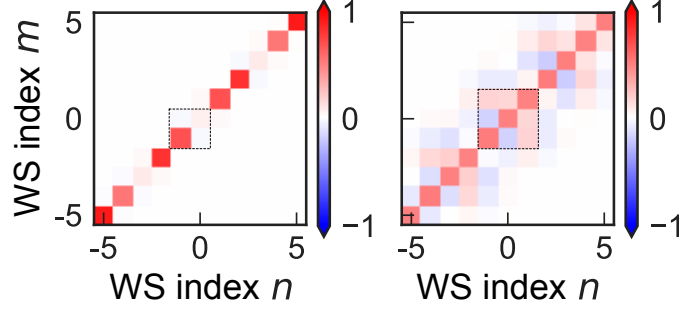


FIG. S1. The coupling coefficient  $J_{m,n}$  for  $^{87}\text{Rb}$  atoms ( $\lambda_l = 532$  nm,  $\lambda_c = 780$  nm). Left:  $V_0 = 20E_R$  and right:  $V_0 = 6E_R$ . Start from  $|\phi_0\rangle$ , the many-body dynamics mainly happens within the dashed square for either two-level model (left, deep lattice region for dynamical phase transitions) and three-level model (right, shallow lattice region for amplification of Bloch oscillations).

The field operator, when written in the WS basis takes the form,  $\hat{\psi}_g(z) = \sum_n \hat{c}_n \phi_n(z)$ , where  $\hat{c}_n$  annihilates an atom in the state  $|\phi_n\rangle$ . In this basis we can rewrite the Hamiltonian [Eq. (S6)] as:

$$\hat{H}/\hbar = -\Delta_c \hat{a}^\dagger \hat{a} + \eta_p \hat{a}^\dagger + \eta_p^* \hat{a} + \frac{\mathcal{G}_0^2}{\Delta_0} \hat{a}^\dagger \hat{a} \sum_{m,n} J_{m,n} \hat{c}_m^\dagger \hat{c}_n + \omega_B \sum_n n \hat{c}_n^\dagger \hat{c}_n, \quad (\text{S8})$$

where  $J_{m,n} = \int dz \phi_m(z) \phi_n(z) \sin^2 k_c z$  describes the overlap between the WS states  $|\phi_m\rangle, |\phi_n\rangle$  weighted by the cavity field mode function. In Fig. S1 we show the value of these couplings for the typical lattice depths we work in this paper. We define the effective particle number:

$$\hat{N}_{\text{eff}} = \sum_{m,n} J_{m,n} \hat{c}_m^\dagger \hat{c}_n, \quad (\text{S9})$$

as the effective number of atoms coupled to the cavity, which shifts the cavity resonance frequency by  $\mathcal{G}_0^2 \langle \hat{N}_{\text{eff}} \rangle / \Delta_0$ .

### B. Adiabatic elimination of cavity field

Here we study the dynamics via Heisenberg equations of motion using a Markovian approximation. We adiabatic eliminate the cavity field using the fact that  $\Delta_c$  sets the largest frequency scale and derive the effective atom-only Hamiltonian. To do that, we formally integrate the Heisenberg equation of motion of the cavity mode operator  $\hat{a}$  and photon number operators  $\hat{a}^\dagger \hat{a}$ , then plug them back into the Hamiltonian [Eq. (S8)]. We remove the fast rotating terms which relax much faster than the time it takes an atom to perform a BO.

The Heisenberg-Langevin equation of the motion for the cavity mode  $\hat{a}$  is given by:

$$\frac{d}{dt} \hat{a} = i[\hat{H}/\hbar, \hat{a}] + \left(\frac{\kappa}{2} \hat{a}^\dagger + \hat{f}^\dagger\right)[\hat{a}, \hat{a}] - [\hat{a}, \hat{a}^\dagger] \left(\frac{\kappa}{2} \hat{a} + \hat{f}\right) = i\left(\Delta_c - \frac{\mathcal{G}_0^2 \hat{N}_{\text{eff}}}{\Delta_0}\right) \hat{a} - i\eta_p - \frac{\kappa}{2} \hat{a} + \hat{f}, \quad (\text{S10})$$

with  $\kappa$  for the cavity decay rate. The above equation captures the dissipative dynamics generated by  $\kappa$  along with the quantum Langevin noise operator  $\hat{f}$ , which gives the formal solution for the cavity field operator:

$$\begin{aligned} \hat{a} &= -i\eta_p \exp \left[ i \int_0^t d\tau \left( \hat{\Delta} + i\kappa/2 \right) \right] \int_0^t dt' \exp \left[ -i \int_0^{t'} d\tau \left( \hat{\Delta} + i\kappa/2 \right) \right] + \hat{f}' \\ &\approx \frac{\eta_p}{\hat{\Delta} + i\kappa/2} + \hat{f}' \end{aligned} \quad (\text{S11})$$

with

$$\hat{\Delta} = \Delta_c - \frac{\mathcal{G}_0^2 \hat{N}_{\text{eff}}}{\Delta_0}, \quad (\text{S12})$$



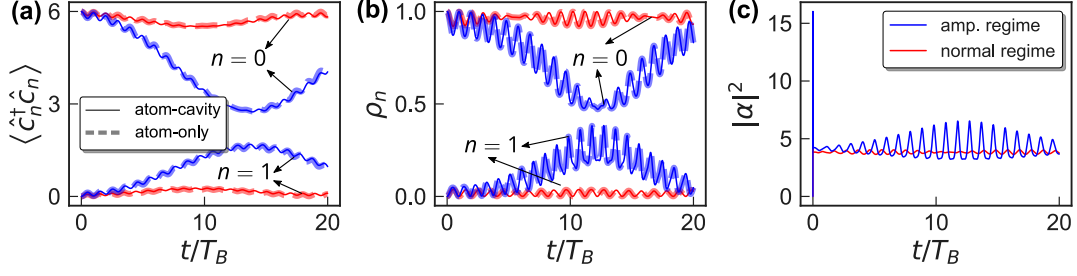


FIG. S2. Benchmarks of the atom-cavity Hamiltonian [Eq. (S8)] with the effective atom-only Hamiltonian [Eq. (S14)]. The red curves for  $V_0 = 5.8E_R$  (normal regime) and the blue curves for  $V_0 = 6.2E_R$  (amplification regime) are used for all the simulations in the figure. (a) Exact Diagonalization (ED) simulation of the dynamics for 6 particles in 3 WS states with the initial state  $(\hat{c}_0^\dagger)^6 |\text{vac}\rangle$ . Populations  $\langle \hat{c}_n^\dagger \hat{c}_n \rangle$  (start from 6) as well as  $\langle \hat{c}_1^\dagger \hat{c}_1 \rangle$  (start from 0) for these two lattice depths are plotted. The solid lines are the exact simulations under the Hamiltonian Eq. (S8) (with the photon space  $n_{\text{cut}} = 10$ ) and the dashed lines under the Hamiltonian Eq. (S14). (b) Mean-field dynamics of  $\rho_n$  with initial state  $|\phi_0\rangle$ . The solid lines are simulated with the atom-cavity mean-field equations of motion [Eq. (S18)] and the dashed lines are simulated with atom-only equations of motion [Eq. (S17)]. Populations  $\rho_0$  (start from 1) as well as  $\rho_1$  (start from 0) for these two parameters are plotted. The differences between the atom-cavity and atom-only simulations can be ignored for both (a) and (b). (c) Mean-field evolution for the cavity photon number with the same parameters for the red and blue curves as in (b).

Here  $\hat{f}'$  is another quantum Langevin noise operator. Below we consider the regime  $\Delta_c, \kappa \gg \omega_B$  where the cavity-field dynamics evolve much faster than the atomic dynamics, thus it follows the latter adiabatically. As a result, we can obtain the formal solution for the cavity photon number operator:

$$\hat{a}^\dagger \hat{a} = \frac{|\eta_p|^2}{\hat{\Delta}^2 + (\kappa/2)^2} + \hat{g} \approx \frac{|\eta_p|^2}{\hat{\Delta}^2}. \quad (\text{S13})$$

One more time  $\hat{g}$  represents a different quantum Langevin noise operator. For the last approximation above, we focus of the regime  $\Delta_c \gg \kappa$  where the unitary dynamics dominates and we can ignore the dissipation process to leading order.

If we insert the above solution of the cavity field into Eq. (S8), the effective atom-only Hamiltonian in the Schrodinger picture can be written as:

$$\begin{aligned} \hat{H}_{\text{eff}}/\hbar &= \omega_B \sum_n n \hat{c}_n^\dagger \hat{c}_n + \eta_p \frac{\eta_p^*}{\hat{\Delta}} + \eta_p^* \frac{\eta_p}{\hat{\Delta}} + \left( \mathcal{G}_0^2 \hat{N}_{\text{eff}}/\Delta_0 - \Delta_c \right) \frac{|\eta_p|^2}{\hat{\Delta}^2} \\ &= \omega_B \sum_n n \hat{c}_n^\dagger \hat{c}_n + 2 \frac{|\eta_p|^2}{\hat{\Delta}} - \hat{\Delta} \frac{|\eta_p|^2}{\hat{\Delta}^2} \\ &= \omega_B \sum_n n \hat{c}_n^\dagger \hat{c}_n + \frac{|\eta_p|^2}{\Delta_c - \mathcal{G}_0^2 \hat{N}_{\text{eff}}/\Delta_0} \\ &\equiv \omega_B \sum_n n \hat{c}_n^\dagger \hat{c}_n + \hat{V}_{\text{cav}}(\hat{N}_{\text{eff}}) \end{aligned} \quad (\text{S14})$$

where  $\hat{V}_{\text{cav}}(\hat{N}_{\text{eff}}) = -(VN/\beta)/(1 + \beta \hat{N}_{\text{eff}}/N)$  is the dynamical potential induced by the cavity which depends on the atomic motion.  $\hat{V}_{\text{cav}}$  is parameterized by the maximum AC Stark shift introduced by the bare cavity mode,  $V = \mathcal{G}_0^2 |\eta_p|^2 / (\Delta_c^2 \Delta_0)$ , as well as by the ratio between the maximum cavity shift and the bare cavity detuning,  $\beta = -N \mathcal{G}_0^2 / (\Delta_0 \Delta_c)$ . We assume  $\beta > 0$  ( $\Delta_0$  and  $\Delta_c$  have opposite signs) to avoid hitting a resonance.

As a benchmark for the effective atom-only Hamiltonian derived in Eq. (S14), we compare the exact dynamics for 6 particles in 3 WS states under Eq. (S8) and Eq. (S14) in Fig. S2(a). In the simulation, we choose  $\Delta_c = 400\omega_B$ ,  $\kappa = 20\Delta_c$ ,  $\eta_p = \Delta_c/10$  as well as  $\mathcal{G}_0^2/\Delta_0 = -100\omega_B$  in the atom-cavity simulation (dashed lines), which corresponds to  $V = \mathcal{G}_0^2 |\eta_p|^2 / (\Delta_c^2 \Delta_0) = \omega_B$  and  $\beta = -N \mathcal{G}_0^2 / (\Delta_0 \Delta_c) = 1.5$  in the atom-only simulation (solid lines). The simulation results match well with each other for the lattice depth in the normal regime (red curves) and amplification regime (blue curves), which verify the effectiveness of the atom-only Hamiltonian.

### C. Equations of motion for atoms

To simulate the dynamics under Eq. (S14), we can calculate the equations of motion for the field operators  $\hat{c}_m$  as:

$$\begin{aligned} i\dot{\hat{c}}_m &= m\omega_B \hat{c}_m - \frac{VN}{\beta} \left[ \hat{c}_m, \frac{1}{(1 + \beta \hat{N}_{\text{eff}}/N)} \right] \\ &= m\omega_B \hat{c}_m - \frac{VN}{\beta} \left[ \hat{c}_m, 1 - \frac{\beta}{N} \hat{N}_{\text{eff}} + \left(\frac{\beta}{N}\right)^2 \hat{N}_{\text{eff}}^2 - \left(\frac{\beta}{N}\right)^3 \hat{N}_{\text{eff}}^3 + \dots \right], \end{aligned} \quad (\text{S15})$$

Then we can simplify the equations above with  $[\hat{c}_m, \sum_{p,q} J_{p,q} \hat{c}_p^\dagger \hat{c}_q] = \sum_n J_{m,n} \hat{c}_n$ :

$$\begin{aligned} i\dot{\hat{c}}_m &= m\omega_B \hat{c}_m - \frac{VN}{\beta} \left\{ -\frac{\beta}{N} [\hat{c}_m, \hat{N}_{\text{eff}}] + \left(\frac{\beta}{N}\right)^2 [\hat{c}_m, \hat{N}_{\text{eff}}^2] - \left(\frac{\beta}{N}\right)^3 [\hat{c}_m, \hat{N}_{\text{eff}}^3] + \dots \right\} \\ &= m\omega_B \hat{c}_m - \frac{VN}{\beta} \left\{ -\frac{\beta}{N} \sum_n J_{mn} \hat{c}_n + \left(\frac{\beta}{N}\right)^2 \left( \sum_n J_{mn} \hat{c}_n \hat{N}_{\text{eff}} + \hat{N}_{\text{eff}} \sum_n J_{mn} \hat{c}_n \right) + \dots \right\}. \end{aligned} \quad (\text{S16})$$

Finally, we apply the mean-field approximation to the operators  $\langle \sum_n J_{mn} \hat{c}_n \hat{N}_{\text{eff}} \rangle \approx \langle \sum_n J_{mn} \hat{c}_n \rangle \langle \hat{N}_{\text{eff}} \rangle$ , and obtain the following equations of motion:

$$i \langle \dot{\hat{c}}_m \rangle = m\omega_B \langle \hat{c}_m \rangle + \frac{V}{(1 + \beta \langle \hat{N}_{\text{eff}} \rangle / N)^2} \sum_{m,n} J_{m,n} \langle \hat{c}_n \rangle, \quad (\text{S17})$$

All the results in the main text were obtained by solving the mean-field equations of motion written above.

Meanwhile, the mean-field equations for the atom-cavity Hamiltonian [Eq. (S8)] is given by,

$$\begin{aligned} i\dot{\alpha} &= - \left( \Delta_c + i\frac{\kappa}{2} - \frac{\mathcal{G}_0^2 \langle \hat{N}_{\text{eff}} \rangle}{\Delta_0} \right) \alpha + \eta_p \\ i \langle \dot{\hat{c}}_m \rangle &= m\omega_B \langle \hat{c}_m \rangle + \frac{\mathcal{G}_0^2}{\Delta_0} |\alpha|^2 \sum_{m,n} J_{m,n} \langle \hat{c}_n \rangle, \end{aligned} \quad (\text{S18})$$

with  $\alpha = \langle \hat{a} \rangle$ . We compare the mean-field dynamics Eq. (S17) and Eq. (S18) in Fig. S2(b). In the simulation, we choose reasonable experimental parameters  $N = 2 \times 10^4$  atoms,  $\Delta_c = 2\pi \times 2$  MHz,  $\kappa = \Delta_c/20$ ,  $\eta_p = 3\Delta_c$  as well as  $\mathcal{G}_0^2/\Delta_0 = -2\pi \times 100$  Hz in the atom-cavity simulation [Eq. (S18)], which corresponds to  $V = \mathcal{G}_0^2 |\eta_p|^2 / (\Delta_c^2 \Delta_0) = 1.57\omega_B$  and  $\beta = -N\mathcal{G}_0^2 / (\Delta_0 \Delta_c) = 1$  in the atom-only simulation [Eq. (S17)]. Still, the simulations for both normal regime and amplification regime match with each other pretty well with the difference can be ignored, which again verifies the validation of the effective atom-only Hamiltonian. In Fig. S2(c), we plot the evolution of cavity photon number  $|\alpha|^2$  which follows the atomic motion adiabatically.

## S2. DYNAMICAL PHASE TRANSITION WITH WANNIER-STARK STATES

In this part, we consider the deep lattice regime and discuss how to map the atom-only Hamiltonian to a spin model. As discussed in the main text, for a deep lattice  $V_0 = 20E_R$ , the WS states approach the Wannier orbitals which are localized. The overlap integral  $J_{m,n}$  for  $V_0 = 20E_R$  is shown in the left panel of Fig. S1 with  $J_{0,0} \approx 0 \ll J_{1,1} \approx J_{-1,-1}$  and  $J_{1,0} \approx -J_{0,-1} \approx 0$ . As a result non-trivial dynamics happens only for  $V(J_{n,n} - J_{0,0}) + n\omega_B \approx 0$  when starting from  $|\phi_0\rangle$ . Here we consider  $V > 0$  and deal with two bosonic modes  $\hat{c}_0, \hat{c}_{-1}$ . For simplicity, we define  $\Omega_n = J_{n,n+1}$  as well as  $\Delta_n = (J_{n,n} - J_{0,0})/2$ . The spin operators are defined as follows,

$$\begin{aligned} \hat{S}_x &= \frac{1}{2} (\hat{c}_{-1}^\dagger \hat{c}_0 + \hat{c}_0^\dagger \hat{c}_{-1}) \\ \hat{S}_y &= -\frac{i}{2} (\hat{c}_{-1}^\dagger \hat{c}_0 - \hat{c}_0^\dagger \hat{c}_{-1}) \\ \hat{S}_z &= \frac{1}{2} (\hat{c}_{-1}^\dagger \hat{c}_{-1} - \hat{c}_0^\dagger \hat{c}_0), \end{aligned} \quad (\text{S19})$$

and the total particle number  $\hat{N} = \hat{c}_{-1}^\dagger \hat{c}_{-1} + \hat{c}_0^\dagger \hat{c}_0$ . Such pseudospin operators satisfy the SU(2) algebra and we can rewrite the effective number operator as ( $\bar{\omega} = (J_{-1,-1} + J_{0,0})/2$ ):

$$\hat{N}_{\text{eff}} = 2\Omega_{-1}\hat{S}_x + 2\Delta_{-1}\hat{S}_z + \bar{\omega}N, \quad (\text{S20})$$

as well as the effective spin model from Eq. (S8) in terms only of  $\hat{c}_{-1}$  and  $\hat{c}_0$ :

$$\hat{H}_{\text{eff}}/\hbar = -\omega_B\hat{S}_z + \hat{V}_{\text{cav}}(\hat{N}_{\text{eff}}) \quad (\text{S21})$$

Similar in Eq. (S15), we can derive Heisenberg equations of motion for the collective spin operator  $\hat{S}_{x,y,z}$ . Using the mean-field approximation which neglects the quantum correlation between different spins we obtain,

$$\begin{aligned} \langle \dot{\hat{S}}_x \rangle &= (\omega_B - 2\Delta_{-1}\tilde{V}) \langle \hat{S}_y \rangle \\ \langle \dot{\hat{S}}_y \rangle &= (2\Delta_{-1}\tilde{V} - \omega_B) \langle \hat{S}_x \rangle - 2\Omega_{-1}\tilde{V} \langle \hat{S}_z \rangle \\ \langle \dot{\hat{S}}_z \rangle &= 2\Omega_{-1}\tilde{V} \langle \hat{S}_y \rangle. \end{aligned} \quad (\text{S22})$$

Moreover, if we introduce the mean-field real variable  $s_\alpha = 2 \langle \hat{S}_\alpha \rangle / N$ ,  $\alpha \in \{x, y, z\}$ , the above equations become:

$$\begin{aligned} \dot{s}_x &= (\omega_B - 2\Delta_{-1}\tilde{V})s_y \\ \dot{s}_y &= (2\Delta_{-1}\tilde{V} - \omega_B)s_x - 2\Omega_{-1}\tilde{V}s_z \\ \dot{s}_z &= 2\Omega_{-1}\tilde{V}s_y, \end{aligned} \quad (\text{S23})$$

with

$$\tilde{V} = \frac{V}{(1 + \beta N_{\text{eff}}(t)/N)^2}, \quad (\text{S24})$$

here  $N_{\text{eff}}(t) = N(\Omega_{-1}s_x + \Delta_{-1}s_z + \bar{\omega})$ . Later we will use the symbol  $n_{\text{eff}} \equiv \Omega_{-1}s_x + \Delta_{-1}s_z + \bar{\omega}$  for convenience. We compare the results from Eq. (S17) and Eq. (S23) to numerical simulations of the full Hamiltonian and they match with each other, which means the two-mode approximation works in this case. Now, we discuss the dynamical phase transition predicted by Eq. (S23). Using both energy conservation as well as the identity  $(\hat{S}^x)^2 + (\hat{S}^y)^2 + (\hat{S}^z)^2 = (\frac{N}{2} + 1)\frac{N}{2}$  in the large  $N$  limit, the real variable  $(s_x, s_y, s_z)$  with initial condition  $s_z = -1, s_x = s_y = 0$  satisfy the following two conservation laws:

$$s_x^2 + s_y^2 + s_z^2 = 1 \quad (\text{S25})$$

$$-\omega_B s_z - \frac{2V/\beta}{1 + \beta n_{\text{eff}}} = \omega_B - \frac{2V/\beta}{1 + \beta(\bar{\omega} - \Delta_{-1})}, \quad (\text{S26})$$

then we can express  $s_{x,y,z}$  all as a function of  $n_{\text{eff}}$ :

$$\begin{aligned} s_z(n_{\text{eff}}) &= \frac{F(\bar{\omega} - \Delta_{-1}) - F(n_{\text{eff}})}{\omega_B} - 1 \\ s_x(n_{\text{eff}}) &= \frac{n_{\text{eff}} - \Delta_{-1}s_z(n_{\text{eff}}) - \bar{\omega}}{\Omega_{-1}} \\ s_y^2(n_{\text{eff}}) &= 1 - s_x^2(n_{\text{eff}}) - s_z^2(n_{\text{eff}}), \end{aligned} \quad (\text{S27})$$

also we define a function,

$$F(x) = \frac{2V/\beta}{1 + \beta x}. \quad (\text{S28})$$

The dynamics correspond to a classical particle moving in the external potential from Eq. (S23):

$$(n_{\text{eff}})^2 + f(n_{\text{eff}}) = 0, \quad (\text{S29})$$

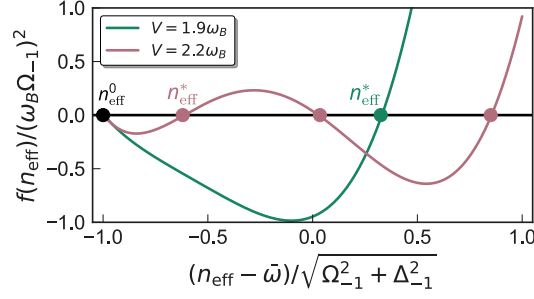


FIG. S3. Number of roots for the effective potential  $f(n_{\text{eff}})$ . In the case of  $V = 1.9\omega_B$ ,  $\beta = 0.5$  (green),  $f(n_{\text{eff}})$  has two roots; In the case of  $V = 2.2\omega_B$ ,  $\beta = 0.5$  (red),  $f(n_{\text{eff}})$  has four roots. The nearest root is labelled by  $n_{\text{eff}}^*$  and the jump of  $n_{\text{eff}}^*$  indicate DPTs.

with the potential  $f(n_{\text{eff}}) = -(\omega_B \Omega_{-1})^2 s_y^2(n_{\text{eff}})$ . The condition  $f(n_{\text{eff}}) = 0$  determines the roots and we find  $n_{\text{eff}}^0 = \bar{\omega} - \Delta_{-1}$  is one of such root. The effective potential can have either two or four solutions within the region  $n_{\text{eff}} \in [\bar{\omega} - \sqrt{\Omega_{-1}^2 - \Delta_{-1}^2}, \bar{\omega} + \sqrt{\Omega_{-1}^2 + \Delta_{-1}^2}]$  shown in Fig. S3, and the dynamics of  $n_{\text{eff}}$  can be understood as the oscillations between  $n_{\text{eff}}^0$  and the nearest root  $n_{\text{eff}}^*$ . Begin with a function  $f(n_{\text{eff}})$  with two roots, and continuously tune the parameters of  $f(n_{\text{eff}})$  so that two new roots appear in between, then a jump of the nearest root  $n_{\text{eff}}^*$  should occur during this process. The dynamical paramagnetic phase corresponds to four roots, while the dynamical ferromagnetic phase corresponds to two roots. Deep in the dynamical paramagnetic phase, one can access the whole Bloch sphere ( $n_{\text{eff}}^* \approx \bar{\omega} + \sqrt{\Omega_{-1}^2 + \Delta_{-1}^2}$ ), while deep in the dynamical ferromagnetic phase, the Bloch vector only cycles around the south pole ( $n_{\text{eff}}^* \approx n_{\text{eff}}^0$ ). By numerically varying  $\beta$  and  $V$ , we compute the number of roots to produce the phase diagram featured in the main text. If  $\beta < 0.32$ ,  $f(n_{\text{eff}})$  can only possess two roots, resulting in a smooth crossover rather than a phase transition.

The LMG model [S1, S2] supports a dynamical phase transition with Hamiltonian:

$$H_{\text{LMG}} = \chi \hat{S}_z^2 + \Omega \hat{S}_x - \delta \hat{S}_z. \quad (\text{S30})$$

To gain more insights on how our model related to the LMG model, we can expand Eq. (S8) to first order and second order in  $(2\Omega_{-1}\hat{S}_x + 2\Delta_{-1}\hat{S}_z)$ . To the first order:

$$\hat{H}_{\text{eff}} = -\omega_B \hat{S}_z + V(2\Omega_{-1}\hat{S}_x + 2\Delta_{-1}\hat{S}_z) - \frac{V\beta}{N}(2\Omega_{-1}\hat{S}_x + 2\Delta_{-1}\hat{S}_z)^2, \quad (\text{S31})$$

If we perform a rotation along y-axis with angle  $\theta = \arctan \Omega_{-1}/\Delta_{-1}$ , then the Hamiltonian become:

$$\begin{aligned} \hat{H}_{\text{eff}} &= -\omega_B \frac{\Delta_{-1}\hat{S}_z - \Omega_{-1}\hat{S}_x}{\sqrt{\Omega_{-1}^2 + \Delta_{-1}^2}} + 2V\sqrt{\Omega_{-1}^2 + \Delta_{-1}^2}\hat{S}_z - 4\frac{V\beta}{N}(\Omega_{-1}^2 + \Delta_{-1}^2)\hat{S}_z^2 \\ &= -4\frac{V\beta}{N}(\Omega_{-1}^2 + \Delta_{-1}^2)\hat{S}_z^2 + \frac{\omega_B\Omega_{-1}}{\sqrt{\Omega_{-1}^2 + \Delta_{-1}^2}}\hat{S}_x - \left(\frac{\omega_B\Delta_{-1}}{\sqrt{\Omega_{-1}^2 + \Delta_{-1}^2}} - 2V_1\sqrt{\Omega_{-1}^2 + \Delta_{-1}^2}\right)\hat{S}_z, \end{aligned} \quad (\text{S32})$$

which takes the form of the LMG model and gives  $\tilde{\chi}$ ,  $\tilde{\Omega}$ ,  $\tilde{\delta}$  defined in the main text.

### S3. SCHWINGER BOSONS AND UNDEPLETED PUMP APPROXIMATION

In this part, we start with the effective Hamiltonian [Eq. (S14)], but consider the shallow lattice region around  $6E_R$ . The associated  $J_{m,n}$  couplings are plotted in the right panel of Fig. S1. Instead of being localized in a single lattice site, the WS states can extend over a few adjacent lattice sites in a shallow lattice. This can lead to significant suppression of differential AC Stark shifts (homogeneous  $J_{n,n}$ ) at the so-called magic lattice depth ( $V_0 = 6E_R$  in our case). Note that the energy difference between nearest-neighbour WS states is rough  $\omega_B$ , which allows us to study Bloch oscillations under cavity-mediated interaction. We consider the WS states with index  $m, n \in \{-1, 0, 1\}$  and use

undepleted pump approximation (UPA)  $\hat{c}_0 \approx \sqrt{N}$  which is valid at short times when starting from  $|\phi_0\rangle$ ,

$$\hat{N}_{\text{eff}} \approx 2\Delta_1 \hat{c}_1^\dagger \hat{c}_1 + 2\Delta_{-1} \hat{c}_{-1}^\dagger \hat{c}_{-1} + \sqrt{N}[\Omega_1(\hat{c}_1^\dagger + \hat{c}_1) - \Omega_{-1}(\hat{c}_{-1}^\dagger + \hat{c}_{-1})] + NJ_{0,0} \quad (\text{S33})$$

$$\equiv \hat{O} + NJ_{0,0}. \quad (\text{S34})$$

Since  $\hat{O}$  is small under UPA that assumes the  $\hat{c}_{\pm 1}$  modes remain almost unoccupied, we can expand the effective Hamiltonian [Eq. (S14)] up to second order in  $\hat{O}$ , and ignore the higher-order terms. The term  $\hat{O}^2$  we can be approximated to be:

$$\hat{O}^2 \approx N[\Omega_1(\hat{c}_1^\dagger + \hat{c}_1) - \Omega_{-1}(\hat{c}_{-1}^\dagger + \hat{c}_{-1})]^2, \quad (\text{S35})$$

and then the effective Hamiltonian becomes:

$$\hat{H}_{\text{eff}}/\hbar = \omega_B(\hat{c}_1^\dagger \hat{c}_1 - \hat{c}_{-1}^\dagger \hat{c}_{-1}) - \frac{VN/\beta}{1 + \beta J_{0,0} + \beta \hat{O}/N} \quad (\text{S36})$$

$$\approx \omega_B(\hat{c}_1^\dagger \hat{c}_1 - \hat{c}_{-1}^\dagger \hat{c}_{-1}) + V_1 \hat{O} + V_2 \hat{O}^2 \quad (\text{S37})$$

$$= \omega_B(\hat{c}_1^\dagger \hat{c}_1 - \hat{c}_{-1}^\dagger \hat{c}_{-1}) + V_1 \sqrt{N}[\Omega_1(\hat{c}_1^\dagger + \hat{c}_1) - \Omega_{-1}(\hat{c}_{-1}^\dagger + \hat{c}_{-1})] \quad (\text{S38})$$

$$+ V_1(\Delta_1 \hat{c}_1^\dagger \hat{c}_1 + \Delta_{-1} \hat{c}_{-1}^\dagger \hat{c}_{-1}) + V_2 N[\Omega_1(\hat{c}_1^\dagger + \hat{c}_1) - \Omega_{-1}(\hat{c}_{-1}^\dagger + \hat{c}_{-1})]^2, \quad (\text{S39})$$

here

$$V_1 = \frac{2V}{(1 + \beta J_{0,0})^2}, \quad V_2 = -\frac{V\beta/N}{(1 + \beta J_{0,0})^3}. \quad (\text{S40})$$

Moreover, we can absorb the linear term generated by single-particle tunneling via a displacement of a coherent state,  $\hat{c}_{\pm 1} = \alpha_{\pm 1} + \hat{c}'_{\pm 1}$  to obtain,

$$\hat{H}_{\text{eff}}/\hbar \approx \omega_B(\hat{c}'_1 \hat{c}'_1 - \hat{c}'_{-1} \hat{c}'_{-1}) + V_1 \Delta(\hat{c}'_1 \hat{c}'_1 + \hat{c}'_{-1} \hat{c}'_{-1}) + V_2 N \Omega^2 (\hat{c}'_1 + \hat{c}'_1 - \hat{c}'_{-1} - \hat{c}'_{-1})^2 \quad (\text{S41})$$

here we have made the approximation  $\Omega_1 \equiv \Omega \approx -\Omega_{-1}$  as well as  $\Delta_1 \equiv \Delta = \Delta_{-1}$ . The displacements then become,

$$\alpha_1 = \frac{V_1 \sqrt{N} \Omega (V_1 \Delta - \omega_B)}{(V_1 \Delta)^2 - \omega_B^2 - 8\Omega^2 V_2 N \omega_B}, \quad \alpha_{-1} = \frac{V_1 \sqrt{N} \Omega (V_1 \Delta + \omega_B)}{(V_1 \Delta)^2 - \omega_B^2 - 8\Omega^2 V_2 N \omega_B} \quad (\text{S42})$$

The short-time dynamics [Eq. (S39)] can be calculated analytically for the quadratic Hamiltonian in terms of  $\hat{c}'_{\pm 1}, \hat{c}'_{\pm 1}^\dagger$  with  $\hat{c}'_{\pm 1} = i[\hat{H}_{\text{eff}}/\hbar, \hat{c}_{\pm 1}]$  and  $\hat{c}'_{\pm 1}^\dagger = i[\hat{H}_{\text{eff}}/\hbar, \hat{c}_{\pm 1}^\dagger]$ . In this limit the dynamics is given by the equation:

$$i \begin{pmatrix} \dot{\hat{c}}'_1 \\ \dot{\hat{c}}'_{-1} \\ \dot{\hat{c}}'^{\dagger}_1 \\ \dot{\hat{c}}'^{\dagger}_{-1} \end{pmatrix} = \mathcal{H}_{\text{BdG}} \begin{pmatrix} \hat{c}'_1 \\ \hat{c}'_{-1} \\ \hat{c}'^{\dagger}_1 \\ \hat{c}'^{\dagger}_{-1} \end{pmatrix}, \quad (\text{S43})$$

with the coupling matrix  $S$ :

$$\mathcal{H}_{\text{BdG}} = \begin{pmatrix} \omega_B + V_1 \Delta + 2V_2 \Omega^2 & 2V_2 \Omega^2 & -2V_2 \Omega^2 & -2V_2 \Omega^2 \\ -2V_2 \Omega^2 & -2V_2 \Omega^2 & -\omega_B + V_1 \Delta + 2V_2 \Omega^2 & 2V_2 \Omega^2 \\ -2V_2 \Omega^2 & -\omega_B - V_1 \Delta - 2V_2 \Omega^2 & 2V_2 \Omega^2 & 2V_2 \Omega^2 \\ 2V_2 \Omega^2 & 2V_2 \Omega^2 & -2V_2 \Omega^2 & \omega_B - V_1 \Delta - 2V_2 \Omega^2 \end{pmatrix}. \quad (\text{S44})$$

The matrix  $\mathcal{H}_{\text{BdG}}$  can have either real or complex eigenvalues, which leads to distinct dynamical behaviors as shown in the main text. When all the eigenvalues are real, the populations  $\rho_{\pm 1}$ , with  $\rho_n = \langle \hat{c}_n^\dagger \hat{c}_n \rangle$ , feature stable small amplitude oscillations; on the other hand when all the eigenvalues are complex, then  $\rho_{\pm 1}$  feature an exponential growth associated with the correlated pair production of atoms at WS centered at  $n = \pm 1$ , which leads to the amplification of the Bloch oscillation signal until the UPA breaks down.



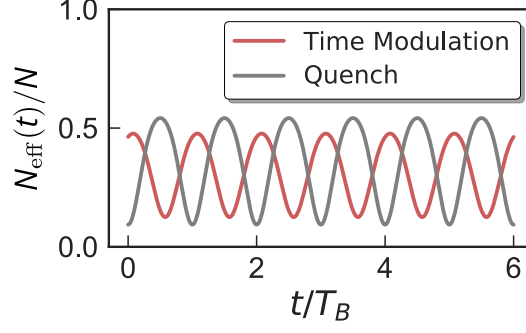


FIG. S4. Single particle Bloch oscillation with amplitude modulation scheme (pink curve,  $V_0 = 8E_R$  and  $V_1 = 0.4E_R$ ) and Quench scheme (grey curve, quench from  $V_0 = 15E_R$  to  $V_0 = 8E_R$  as main text).

#### S4. EXPERIMENTAL CONSIDERATIONS

##### A. Single-particle Bloch oscillations

In this section, we discuss the protocols to observe single-particle Bloch oscillations in the experiment. The main idea is to prepare a superposition of different WS states which accumulate different phases under  $\hat{H}_0$ . In the main text, we discussed the quench scheme where the initial localized WS state  $\phi_0$  becomes a superposition of delocalized WS states. An alternative way to probe Bloch oscillations is to amplitude modulate the lattice depth as:

$$\begin{aligned} H_1(t)/\hbar &= V_1 \sin^2 k_l z \cos(\omega t + \phi) \\ &= \sum_{m,n=-\infty}^{\infty} t_m \cos(\omega t + \phi) (\hat{c}_{m+n}^\dagger \hat{c}_n + \hat{c}_n^\dagger \hat{c}_{m+n}), \end{aligned} \quad (\text{S45})$$

which has been demonstrated in [S3]. Here we define the tunnelling rate between  $\phi_{m+n}$  and  $\phi_n$  as:

$$t_m = V_1 \int dz \sin^2(k_l z) \phi_{m+n}(z) \phi_n(z), \quad (\text{S46})$$

Moreover, we can choose  $\omega \approx m\omega_B, m \in \mathbb{Z}$  to drive the  $m$ th sideband (between  $\phi_{m+n}$  and  $\phi_n$ ) and ignore the fast rotating terms:

$$\begin{aligned} H_1(t)/\hbar &= \sum_{m,n=-\infty}^{\infty} t_m \cos(\omega t + \phi) (e^{im\omega_B t} \hat{c}_{m+n}^\dagger \hat{c}_n + e^{-im\omega_B t} \hat{c}_n^\dagger \hat{c}_{m+n}) \\ &\approx \sum_{n=-\infty}^{\infty} \frac{t_m}{2} (e^{-i\phi} \hat{c}_{m+n}^\dagger \hat{c}_n + e^{i\phi} \hat{c}_n^\dagger \hat{c}_{m+n}). \end{aligned} \quad (\text{S47})$$

As a result, starting from  $\phi_0$  and performing the amplitude modulation for time  $\tau$ , we obtain the initial state to be a superposition of WS states  $\{\phi_{n \times m}\}$ . In Fig. S4 (pink curve), we simulate the case with lattice depth  $V_0 = 8E_R$  and modulation strength  $V_1 = 0.4E_R$ , also the first sideband transition ( $\omega = \omega_B$ ). Different from the quench scheme (grey curve), after the modulation the single particle wavefunction can have a non-zero coupling to the cavity field ( $N_{\text{eff}}/N \neq 0$ ).

In the experiment, there may be higher bands populated in the quench protocol we discussed in the main text. In other words, the WS basis describing the ground band for the shallow lattice (after quench) is not necessarily complete to describe the initial localized state. Higher bands population will inevitably introduce other frequency components to  $N_{\text{eff}}(t)$  disrupting the BO signal. However, in the simulations we performed for the main text (quench from  $V_0 = 15E_R$  to  $V_0 = 8E_R$ ), 98% atoms remained in the ground band and the higher band population can be ignored. Similarly, in the amplitude modulation schemes, we also choose  $V_1$  to be much smaller than the band gap to avoid higher bands population.

Atomic species	$\lambda_l$ (nm)	$\lambda_c$ (nm)	Magic lattice depth ( $E_R$ )
$^{87}\text{Rb}$ (boson)	532	780	$6E_R$
$^{87}\text{Sr}$ (fermion)	532	689	$5E_R$
$^{88}\text{Sr}$ (boson)	532	689	$5E_R$
$^{171}\text{Yb}$ (fermion)	413	556	$3.2E_R$

TABLE S1. Summarized lattice, cavity wavelength and magic lattice depth for different atomic species.

### B. Experimental parameters

Here we discuss the parameters for the specific case of  $^{87}\text{Rb}$  with incommensurate lattice wavelength ( $\lambda_l = 532$  nm,  $\omega_B = 2\pi \times 557$  Hz) and cavity wavelength ( $D_2$  transition with  $\lambda_c = 780$  nm). We are interested in the parameter regime with  $V \sim \omega_B$  and  $\beta \sim O(1)$ , where the dynamics is mostly unitary and the dissipative processes can be ignored as we explain below. Another requirement is that the band gap ( $27\omega_B$  for  $\lambda_l = 532$  nm and  $V_0 = 6E_R$ ) should be much larger than  $V$  if we want to only work with the ground band WS states. Moreover, the cavity decay rate  $\kappa \sim 2\pi \times 0.1$  MHz, the atom-light coupling strength  $\mathcal{G}_0 \sim 2\pi \times 0.3$  MHz, and atomic transition decay rate  $\gamma \sim 2\pi \times 10$  MHz give the cavity cooperativity  $C = 4\mathcal{G}_0^2/\gamma\kappa \sim 0.36$ , which can be tuned even larger for larger  $\mathcal{G}_0$  and smaller  $\kappa, \gamma$ . The cavity loss generates collective dephasing processes at a rate  $V\beta\kappa/\Delta_c$ , while spontaneous emission generates off-resonant photon scattering processes at a rate  $V\gamma/\Delta_0$  as mentioned in the main text. Under  $\kappa/\Delta_c \sim 0.05$  and  $\gamma/\Delta_0 \sim 0.01$ , one obtains negligible dissipation within the experimentally relevant time scales and  $\beta \sim O(1)$ . For the maximum AC Stark shift, we first find that  $\mathcal{G}_0^2/\Delta_0 \sim 2\pi \times 100$  Hz with the parameters listed above, then  $|\eta_p|^2/\Delta_c^2$  can be tuned between 1 to 10 for  $V \sim \omega_B$ .

Our proposal works with a single internal level in the ground state manifold for atoms hopping between motional states (WS states here). Since interactions are mediated by photons, quantum statistics are not important in our scheme. As a result, even though above we considered the case of Rb, our model can be realized with other species of alkali atoms ( $D_2$  transition) and alkaline earth atoms ( $^1S_0 \rightarrow ^3P_1$  transition) i.e.  $^{87}\text{Sr}$  (boson),  $^{88}\text{Sr}$  (fermion),  $^{171}\text{Yb}$  (fermion) with appropriate choices of lattice wavelength and magic lattice depth summarized in table S1. Note that both  $^{88}\text{Sr}$ ,  $^{171}\text{Yb}$  have very small scattering lengths in the ground states.

The single particle Bloch oscillations and dynamical phase transition in the deep lattice doesn't set too much limit on the choice of  $\lambda_l$  and  $\lambda_c$ . We only want the near-neighbour coupling coefficient  $J_{m,m+1}$  to be larger, while the overlaps between  $\phi_m(z)$ ,  $\phi_{m+1}(z)$  and  $\sin^2(k_c z)$  become tiny when  $\lambda_l \approx \lambda_c$ , so we want to choose different  $\lambda_l$  and  $\lambda_c$ . While for the amplification of BOs in the shallow lattice region, we need to perform the experiment around magic lattice depth thus too shallow magic depth (such as  $^{171}\text{Yb}$ ) isn't favorable.

### C. Radial mode thermal distribution

In this section, we discuss the effect of the Radial thermal motion following Ref. [S4]. The Gaussian geometry of the laser beams in experiments inevitably couples the vertical and radial wave functions. The Gaussian profile of the lattice and cavity beams causes atoms in different radial modes to have different tunneling rate, resulting in a slightly different overlap integral  $J_{m,n}$  for atoms in different radial modes. This effect can also be understood as fluctuations of the lattice potential  $V_0$  due to radial thermal excitation.

First, we focus on the Gaussian beam profile of a 1D lattice, which leads to the following trapping potential:

$$V_0(r, z) = V_0 \sin^2(k_l z) \exp(-2r^2/w_l^2), \quad (\text{S48})$$

where  $w_l$  is the beam width. In the presence of additional radial trapping potential  $V_r(r, z) = M\omega_r^2 r^2/2$  [S5] we can expand the total trapping potential  $V(r, z) = V_0(r, z) + V_r(r, z)$  to second order of  $r$  and obtain:

$$V(r, z) \approx V_0 \sin^2(k_l z) + \frac{1}{2}M\omega_r^2 r^2 - \frac{\omega_{r0}^2}{\omega_r^2} \frac{1}{2}M\omega_r^2 r^2 \sin^2(k_l z), \quad (\text{S49})$$

here  $\omega_{r0} = \sqrt{4V_0/Mw_l^2}$ .

The first term describes the lattice potential along the axial direction with the characteristic Bloch functions as eigenstates. The second term describes the radial harmonic trapping with eigenstate  $\phi_{n_x, n_y}(r) = \phi_{n_x}(x)\phi_{n_y}(y)$  and

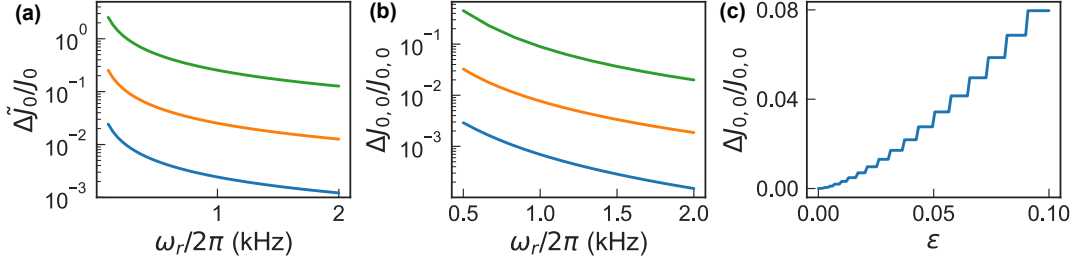


FIG. S5. The standard deviations of (a) the ground band tunneling rates, (b) the coupling coefficient  $J_{0,0}$  as a function of radial trapping  $\omega_r$  with fixed  $T = 0.1 \mu\text{K}$  (blue curve),  $T = 1 \mu\text{K}$  (orange curve) as well as  $T = 10 \mu\text{K}$  (green curve). We use the beam width  $w_l = 50 \mu\text{m}$  and lattice potential  $V_0 = 6E_R$  in the calculation. (c) The standard deviations of  $J_{0,0}$  as a function of loading error rate  $\epsilon$ .

eigenenergies  $E_{n_x, n_y} = \hbar\omega_r(n_x + n_y + 1/2)$ . The third term describes the coupling between axial and radial degrees of freedom. The correction of  $J_0$  is given by [S4]:

$$\tilde{J}_0(n_x, n_y) = J_0 + \frac{1}{8} \frac{\omega_{r0}^2}{\omega_r^2} E_{n_x, n_y} \left[ \frac{\partial}{\partial v_0} f(\tilde{q} = 0, v_0/4) - \frac{\partial}{\partial v_0} f(\tilde{q} = \pm 1, v_0/4) \right]. \quad (\text{S50})$$

Here the function  $f$  is the characteristic Mathieu value of type A for  $q \in (-\hbar k_l, \hbar k_l)$ , and the characteristic Mathieu value of type B for  $q = \pm k_l$ . We define  $\tilde{q} = q/\hbar k_l$  and  $v_0 = V_0/E_R$ . One can take such  $\tilde{J}_0$  into Eq. (S7) to calculate  $\phi_n(z)$ , which causes inhomogeneity for the coupling matrix  $J_{m,n}$ . We can estimate the contribution from different radial eigenmode with Boltzmann distribution  $p_{n_x, n_y} = \exp[-(n_x + n_y)\omega_r\hbar/k_B T]/Z$ , in which the partition function  $Z \approx (k_B T/\hbar\omega_r)^2$ . Then we can calculate the variance of the  $\tilde{J}_0$  as:

$$\begin{aligned} \Delta \tilde{J}_0^2 &= \sum_{n_x, n_y} p_{n_x, n_y} [\tilde{J}_0(n_x, n_y) - J_0]^2 \\ &= \left\{ \frac{\hbar \omega_{r0}^2}{8 \omega_r} \left[ \frac{\partial}{\partial v_0} f(\tilde{q} = 0, v_0/4) - \frac{\partial}{\partial v_0} f(\tilde{q} = \pm 1, v_0/4) \right] \right\}^2 \frac{2(e^{\hbar\omega_r/k_B T} + 2)}{(e^{\hbar\omega_r/k_B T} - 1)^2}. \end{aligned} \quad (\text{S51})$$

In Fig. S5(a), we plot the standard deviation of the tunneling rate  $J_0$  as a function of  $\omega_r$  and different temperature  $T$ . In Fig. S5(b), we plot the standard deviation of the coupling coefficient  $J_{0,0}$  due to the correction of the tunneling rate. Similar behavior for other coupling coefficients  $J_{m,n}$ . As a result, one can suppress the effect of the radial modes occupation by increasing the total radial trapping frequency  $\omega_r$  or lowering the temperature. The standard deviation  $\Delta J_{0,0} \approx 0.01 J_{0,0}$  up to temperature  $T \sim 1 \mu\text{K}$  as well as  $\omega_r = 2\pi \times 1 \text{ kHz}$ , thus the radial thermal noise only has a tiny effect on many-body dynamics we predict.

#### D. Atoms loading

In this section, we discuss the real process of atoms loading in the experiment. In the main text, we mention first loading atoms at position  $k_c z/\pi = r, r \in \mathbb{Z}$  which atoms-cavity coupling becomes perfect zero. However one can only set a threshold for the atom-cavity coupling during the loading process i.e. load all the atoms with  $\sin^2 k_c z < \epsilon$  in the real experiment. Such loading error makes  $J_{m,n}$  deviate from expected values, which brings additional inhomogeneity. In Fig. S5(c), we plot the standard deviation of the coupling coefficient  $J_{0,0}$  as a function of error  $\epsilon$ . We consider the total lattice length to be 1 mm and assume atoms load into all the sites  $n$  which satisfy  $\sin^2(k_c n a_l) < \epsilon$  uniformly. These imperfect sites cause tiny inhomogeneity in the coupling coefficient  $J_{m,n}$  up to  $\epsilon \sim 5\%$ .

- 
- [S1] A. Chu, J. Will, J. Arlt, C. Klempt, and A. M. Rey, Simulation of xxz spin models using sideband transitions in trapped bosonic gases, *Physical Review Letters* **125**, 240504 (2020).  
[S2] J. A. Muniz, D. Barberena, R. J. Lewis-Swan, D. J. Young, J. R. K. Cline, A. M. Rey, and J. K. Thompson, Exploring dynamical phase transitions with cold atoms in an optical cavity, *Nature* **580**, 602 (2020).

- [S3] A. Alberti, G. Ferrari, V. V. Ivanov, M. L. Chiofalo, and G. M. Tino, Atomic wave packets in amplitude-modulated vertical optical lattices, [New Journal of Physics](#) **12**, 065037 (2010).
- [S4] A. Chu, P. He, J. K. Thompson, and A. M. Rey, Quantum enhanced cavity qed interferometer with partially delocalized atoms in lattices, [Physical Review Letters](#) **127**, 210401 (2021).
- [S5] K. C. Cox, G. P. Greve, B. Wu, and J. K. Thompson, Spatially homogeneous entanglement for matter-wave interferometry created with time-averaged measurements, [Physical Review A](#) **94**, 061601 (2016).